Available online at www.sciencedirect.com
SCIENCE DIRECT®
Journal of Nuclear Materials 351 (2006) 162–173
journal of nuclear materials
www.elsevier.com/locate/jnucmat

Microstructural evolution of proton irradiated T91

G. Gupta *, Z. Jiao, A.N. Ham, J.T. Busby [1], G.S. Was

Nuclear and Radiological Engineering Department, University of Michigan, 2940 Cooley Building, 2355 Bonisteel Boulevard, Ann Arbor, MI 48019, USA

Abstract

Understanding radiation effects in ferritic–martensitic alloys is critical for their success in advanced reactor and transmutation systems. The objective of this work is to evaluate the microstructural and mechanical property changes in irradiated ferritic–martensitic alloy T91. Irradiations were conducted with 2.0 MeV protons to doses of 3, 7, and 10 dpa at a dose rate of 2×10^{-5} dpa/s and at temperatures of 400 °C, 450 °C, and 500 °C. The post irradiation microstructure contained a high density of black-dots and $a_0\langle 1\,0\,0\rangle$ dislocation loops in addition to precipitates and tangled dislocations that were present in the unirradiated condition. The irradiated dislocation microstructure is sensitive to the heat treatment. Results show that the irradiated microstructure did not contain any voids or evidence of second phase formation. Hardness increases with dose and tends to saturate around 5 dpa for 400 °C irradiation. Only a portion of irradiation hardening can be accounted for by the observable microstructural features. An initial investigation of the effect of irradiation on prior austenite grain boundary microchemistry revealed that Cr is enriched by 4.7 wt%, V by 0.6 wt% (nearly 300%), and Fe is depleted by 5.3 wt% relative to the bulk values. No segregation was observed in the unirradiated condition. No radiation-induced segregation was observed at martensite lath boundaries. Overall, the irradiated microstructure is consistent with reactor and spallation system experiments.

1. Introduction

Ferritic–martensitic alloys are proposed as candidate structural materials for Generation IV reactors and accelerator-driven transmutation systems (ADS). They are preferred over austenitic stainless steels in these applications due to improved irradiation stability and mechanical properties such as reduced swelling, high temperature creep resistance, and thermal shock resistance. Understanding radiation effects in these alloys is critical for their success in advanced reactor and transmutation systems. These steels have been used in the power-generation, chemical, petrochemical industries and fossil fired power plants at temperatures up to 550–600 °C [1]. Thus, the technology for production and fabrication exists and the unirradiated mechanical properties are well understood. However, the effects of irradiation in the environments expected in Generation IV and ADS systems are only partially complete. The objective of this work is to evaluate the microstructural, microchemical, and mechanical property changes in irradiated

* Corresponding author. Tel.: +1 734 936 0266; fax: +1 734 763 4540.
E-mail address: gauravg@umich.edu (G. Gupta).
[1] Present address: Oak Ridge National Laboratory, 1 Bethel Valley Road, P.O. Box 2008, Oak Ridge, TN 37831, USA.

0022-3115/$ - see front matter © 2006 Elsevier B.V. All rights reserved.
doi:10.1016/j.jnucmat.2006.02.028

ferritic–martensitic alloy T91 to provide a better understanding of its behavior in advanced reactor systems.

T91 is a ferritic–martensitic steel of composition 9Cr–1Mo with minor alloying elements of Ni, Nb, V, and C. The high temperature strength and radiation stability of the alloy makes it an attractive candidate for applications in reactor and spallation environments. A limited number of previous studies have been performed under fast reactor and low-temperature spallation environments [1–5]. Ferritic–martensitic steels are attractive because of their resistance to radiation-induced swelling. The maximum reported swelling for T91 by Gelles [2] is 1.76% at just over 200 dpa at 420 °C. However, fast-reactor irradiations do not produce the large amount of transmutation gases that are associated with spallation environments. No He production took place in the proton irradiations of this study, still irradiations where He and other gases were produced are compared to due to the relatively similar irradiation conditions like alloy, dose and temperature. Hashimoto and Klueh [4] irradiated T91 doped with 2% Ni in the high flux isotope reactor (HFIR) to 12 dpa at 400 °C. T91 and T91 + 2%Ni produced 30 and 161 appm He and exhibited swelling of 0.17% and 0.15%, respectively. Kai and Klueh [3] analyzed the microstructure of T91 irradiated in the fast flux test facility (FFTF) to 35 dpa at a temperature of 420 °C. Post-irradiation microstructure showed a high density of fine voids and large dislocation loops. The $M_{23}C_6$ and MC precipitates were mostly unchanged, showing only minor decreases in number density and increases in diameter. However, the irradiated T91 formed a high density of very fine χ-phase precipitates.

Limited experiments have been performed on T91 under spallation conditions. However, the irradiation temperatures are lower than the expected operating temperatures of Generation IV and future ADS systems. Jia and Dai [5] analyzed T91 irradiated in SINQ Target-3 to doses ranging from 2.7 to 11.8 dpa at temperatures ranging from 90 to 360 °C. The pre-irradiation dislocation density was approximately 10^{14} m^{-2}. $M_{23}C_6$ precipitates were observed primarily along prior austenite and lath boundaries. The precipitate sizes varied from a few tens of nm to ~2 μm in diameter. Due to the nature of the experiment, the fluence and He content increased with irradiation temperature, making it difficult to determine the effects of each parameter individually. At He concentrations above 500 appm, high densities of very fine He bubbles were observed. While the changes were small, a trend of decreasing bubble density and increasing size was observed with increasing dose, He concentration and irradiation temperature. Note here that no He/H production takes place with 2 MeV protons used in this study to irradiate F–M alloy T91. Additionally, dislocation loop size increased with dose/temperature. Jia and Dai observed amorphization of precipitates at temperatures below 250 °C. This is consistent with the observations of Sencer et al. [6] for low-temperature irradiations of T91 at the LANSCE facility.

Several studies have been performed on the response of mechanical properties of T91 to irradiation [7–12]. General trends show an increase in yield strength and ultimate tensile strength and associated decrease in uniform elongation and total elongation with increasing dose. The severity of these changes decrease with increasing temperature. The same trends have been observed with increasing He concentration in implanted samples [13]. Low level damage ($\leqslant$0.8 dpa) occurred due to the He implantation process in the otherwise unirradiated samples.

In the present work, proton irradiations were conducted on alloy T91 to moderate doses (up to 10 dpa) at 400 °C, 450 °C, and 500 °C. Proton irradiation has proven to be an extremely effective tool in emulating the effects of neutron irradiation in austenitic stainless steel used in light water reactor cores [14]. Radiation-induced segregation, dislocation microstructure, irradiation hardening, void formation and susceptibility to irradiation assisted stress corrosion cracking are all properties that have been shown to be emulated by proton irradiation [14]. This investigation will serve to generate baseline data on irradiation effects on T91 in an effort to learn how this alloy responds to irradiation and how the microstructure develops with dose and temperature. Results of microstructural evolution and hardness changes due to irradiation are presented. Additionally, an initial investigation of the effect of irradiation on grain boundary microchemistry is presented.

2. Experiment

2.1. Material and sample fabrication

Two heats of T91 were used in these experiments. The compositions of the T91 alloys are given in Table 1. The alloys were used in the normalized and tempered condition, as noted in Table 1.

Table 1
Composition of T91 Heats A and B in wt%

Heat	Cr	Mo	Mn	V	Nb	Ni	Si	Cu	C	P	Al	S	N	Fe
A[a]	8.13	0.98	0.43	0.24	0.24	0.22	0.27	0.16	0.09	0.09	0.015	<0.01	<0.005	Bal.
B[b]	8.37	0.90	0.45	0.216	0.076	0.21	0.28	0.17	0.10	0.009	0.022	0.003	0.048	Bal.

[a] Normalization: 1038 °C, 1 h; temperature: 740 °C, 45 min [2].
[b] Normalization: 1066 °C, 46 min – air cooled; temperature: 790 °C, 42 min – air cooled.

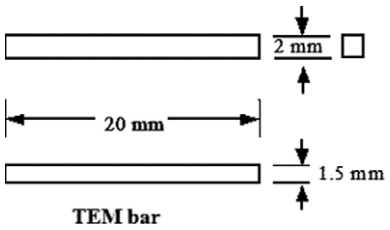

Fig. 1. Schematic of TEM bar sample geometry.

Samples in the form of rectangular bars (designated as 'TEM bars'), 20 mm × 2 mm × 1.5 mm, were fabricated via electric discharge machining, Fig. 1. Since the irradiated region is 10 nm in length, a maximum of three TEM discs can be cut from the surface of each bar. Up to eight bars of this size were irradiated at once, providing consistency of irradiation conditions among the samples. The present work includes samples from three sets of irradiations. Samples for the 450 °C irradiation were machined from Heat A. Samples for the 400 °C and 500 °C irradiations were machined from Heat B. The difference in alloy heats is due to the samples from 450 °C irradiation being from a previous study [15] performed at the Michigan Ion Beam Laboratory, which obtained its alloy from a different source from the more recent 400 °C and 500 °C irradiations.

2.2. Proton irradiation

Proton irradiations were performed using a specially designed stage connected to the General Ionex Tandetron accelerator at the Michigan Ion Beam Laboratory. Irradiations were conducted using 2.0 MeV protons at a dose rate of approximately 2×10^{-5} dpa/s (the experimental doses and dose rates are calculated using the SRIM2003 simulation [15]), resulting in a nearly uniform damage rate through the first 15 μm of the proton range (20 μm), where dpa is calculated using SRIM with a displacement energy of 40 eV. The calculated dose rate is plotted as a function of depth in Fig. 2. Irradiations were conducted to 3, 7, and 10 dpa at 400 °C, 450 °C, and 500 °C.

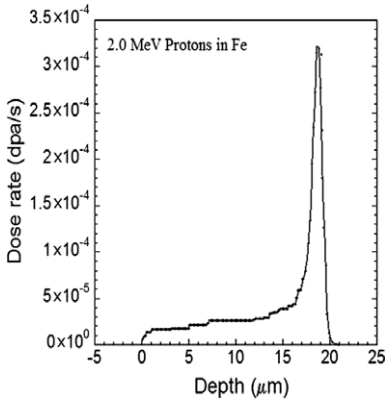

Fig. 2. Damage rate depth profile for Fe irradiated with 2.0 MeV protons as modeled by SRIM2003 [15].

The irradiation stage was designed to control the sample temperature by controlling the stage temperature. The stage was heated using a resistive cartridge heater and cooled using room temperature air flowing through cooling lines that penetrated the back of the stage. The stage surface is made of copper to provide good heat conduction away from the samples. To provide effective thermal contact between the sample bars and the stage, a thin layer of either indium (400 °C and 450 °C irradiations) or tin (500 °C irradiations) was placed between the samples and the stage surface. These metals are molten at the irradiation temperature, maximizing the thermal contact between samples and stage.

During irradiation, sample temperature was monitored continuously using a high-resolution two-dimensional, thermal imaging system (pyrometer) that was pre-calibrated with a set of thermocouples attached to the samples. The imager was configured so that each sample being irradiated was monitored by three areas-of-interest (AOIs) at the top, center and bottom of the irradiated face of the sample. The pyrometer AOIs were calibrated prior to irradiation by heating the samples with the cartridge heater to the set-point temperature and

adjusting the AOI's emissivity setting so that the pyrometer reading matched that of the thermocouples. During irradiation, the sample temperature was controlled to within ±10 °C of the set point temperature by controlling the amount of heating and/or cooling provided to the stage. By providing a large fraction of the total heat input to the samples from the cartridge heater, temperature fluctuations due to fluctuations in beam current were minimized.

The irradiation stage was electrically isolated from the beam line and four rectangular tantalum apertures were used to define the area on the sample bars that was irradiated (10 mm in height by 18 mm in width, which ensured the full width of all samples were irradiated evenly) with the proton beam. The approximately 3 mm diameter proton beam was raster-scanned across the stage so that between one-half and two-thirds of the total beam current was deposited on the samples and the remainder on the apertures. Raster-scanning ensured that all regions of the samples received the same dose. Independent apertures on each side of the rectangular irradiation region permitted precise beam alignment.

Experimental parameters were tracked continuously during irradiation using a PC-based monitoring system. The monitoring software recorded the stage current, the current for each of the apertures, pyrometer temperatures and up to five thermocouple temperatures. This system allowed the operator to continuously monitor experimental parameters while also providing a comprehensive history of each irradiation. Alarms were installed to alert the operator when experimental parameters moved outside acceptable limits.

The proton irradiations were conducted in two parts; a 3.0 dpa irradiation followed by a 7.0 dpa irradiation. For the 400 °C irradiations, the total current (stage plus aperture) was approximately 66 μA. The sample temperature was maintained within ±10 °C during the combined 290-h irradiation (84 h for 3 dpa and 206 h for 7 dpa). For the 500 °C irradiations, the total current was approximately 60 μA. The sample temperature was maintained within ±10 °C during the combine 260-h irradiation (80 h for 3 dpa and 180 h for 7 dpa). Details on the 450 °C irradiations are presented in Ref. [16].

2.3. Microstructure analysis

The irradiated TEM bars were first cut parallel to the irradiated surface, and then mechanically polished from the unirradiated side down to a thickness of approximately 100 μm. A 3 mm diameter slurry cutter was used to cut the TEM discs from the 100 μm thick bars. A solution of 5% perchloric acid in methanol at a temperature of approximately −50 °C was used for jet electro-polishing. The disc was jet-polished from the unirradiated side to perforation. Microstructural characterization was conducted in a JEOL 2010F analytical TEM (FEG-STEM, 200 keV). Two-beam conditions with $\mathbf{g} = [0\,0\,2]$ and $[1\,1\,2]$ near $\langle 1\,1\,0\rangle$ zone axis were set up for bright field imaging. The combination of these two conditions should reveal all dislocations with $\mathbf{b} = a_0/2\langle 1\,1\,1\rangle$ and $\mathbf{b} = a_0\langle 1\,0\,0\rangle$. The radiation-induced cavities were examined in conventional bright field mode under slightly underfocused conditions.

There were eight sample conditions analyzed for alloy T91; unirradiated; irradiated to 3 dpa, 7 dpa and 10 dpa at 400 °C; irradiated to 3 dpa and 10 dpa at 450 °C; and irradiated to 3 dpa and 7 dpa at 500 °C. Note here that the unirradiated sample was from Heat B. Dislocation loop size and number density, dislocation network and radiation-induced cavities were examined in bright-field mode, and lath and precipitate sizes were measured.

2.4. Hardness measurement

Microhardness was measured both prior to and after irradiation by protons. Vickers hardness was measured using a Vickers Microhardness Tester (Micromet-II). Indents were made with a load of 25 g on a TEM bar in both the irradiated region and the unirradiated region. Since proton irradiation produces a fairly uniform damage layer over approximately the first 15 μm, a low load of 25 g with load time of 20 s was applied to ensure that the unirradiated material below the damaged layer was not being sampled (the depth of penetration is approximately 3 μm). The center-to-center spacing of indents was approximately 100 μm, so that specimen deformation from one indent does not affect results from nearby indentations.

2.5. Grain boundary microchemical analysis

Microchemical analysis was performed on unirradiated T91 and a sample irradiated to 10 dpa at 450 °C. Analysis was conducted in a scanning transmission electron microscope with energy-dispersive X-ray analysis (STEM/EDS). The STEM/EDS

analysis of the grain boundaries for the irradiated sample was performed on a Philips CM200/FEG at Oak Ridge National Laboratory, which produces a probe approximately 0.9–1.0 nm in diameter (full-width, half-maximum) while operating at 200 kV. STEM/EDS analyses for the unirradiated sample and the lath boundaries of the 10 dpa sample were performed on a JEOL 2010F at the University of Michigan Electron Microbeam Analysis Laboratory, which produces a probe approximately 0.5 nm in diameter (full-width, half-maximum) while operating at 200 kV. STEM/EDX profiles for the same grain boundary of the 10 dpa sample were collected using both microscopes and compared to verify equivalency, allowing comparison of data between the two instruments.

STEM/EDS measurements were performed on 'edge-on' grain boundaries so as to minimize broadening of the boundary profile. Details of the grain boundary measurement technique are given in Ref. [17]. Measurements were made at 1.5 nm increments along a 45 nm line perpendicular to the grain boundary. Three line measurements were performed on one grain boundary (GB). *k*-factors, which relate the measured X-ray intensity to the local chemical composition, were determined as presented in Ref. [18] by using 6 points on either end of the line scan and the bulk composition of the alloy (determined using electron microprobe) and averaged. Concentrations of Fe, Cr, Mo, Mn, and V were calculated at each point along the line scans from these *k*-factors.

3. Results

3.1. Microstructure

The microstructure of unirradiated T91 contains martensite laths (Fig. 3(a)), precipitates and dislocation cells (Fig. 3(b)), and a sparse dislocation network (Fig. 3(c)). Precipitates are located preferentially at grain boundaries, and also at lath boundaries and in the matrix. Dislocation density varied dramatically, ranging from dislocation-free areas to dense tangles in dislocation cell walls that contain a dislocation density of approximately 5.6×10^{13} m^{-2}.

The irradiated microstructure consisted of a high density of black dots and dislocation loops of type $a_0\langle 1\,0\,0\rangle$, for irradiation temperatures of 400 °C and 450 °C. No black dot damage was evident for an irradiation temperature of 500 °C. Also large loops of type $a_0\langle 1\,0\,0\rangle$ were present even at a low dose of 3 dpa. No cavities or voids were observed, which confirms the swelling resistance of these alloys up to 10 dpa. No significant change was observed in the precipitate size and density following proton irradiation up to 10 dpa. Lath size also remained the same. Fig. 4 presents irradiation-induced defect structures in T91 steel irradiated to different doses. Irradiation conditions and defect data obtained from TEM investigations of the samples are listed in Table 2.

At each irradiation temperature, the dislocation loop size and density and dislocation network density all increases with dose. For the sample irradiated to 3 dpa at 450 °C the most prominent microstructural changes were the high density of dislocation loops and the increase of the network dislocation density, as shown in Figs. 4(a) and 5(a). The dislocation microstructure at 10 dpa (Fig. 4(b)) is very similar to that at 3 dpa but with an increase in loop size and loop density. Similar trends were observed for samples at 400 °C and 500 °C with increasing dose. The only difference is the large loop sizes obtained at 500 °C, even at low doses. With an increase in irradiation temperature at the same dose, dislocation loop density and network density decrease while the loop size increases. It should also

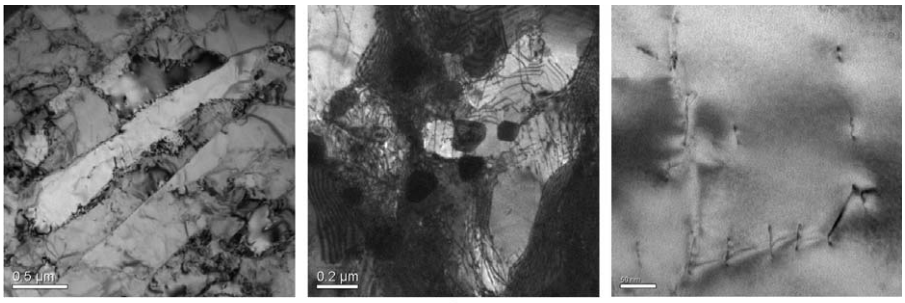

Fig. 3. TEM micrograph of unirradiated T91 showing (a) lath structure, (b) dislocations cells and carbides, and (c) dislocations (diffraction condition of $\mathbf{g} = 1\,1\,0$ near zone [0 0 1] was used).

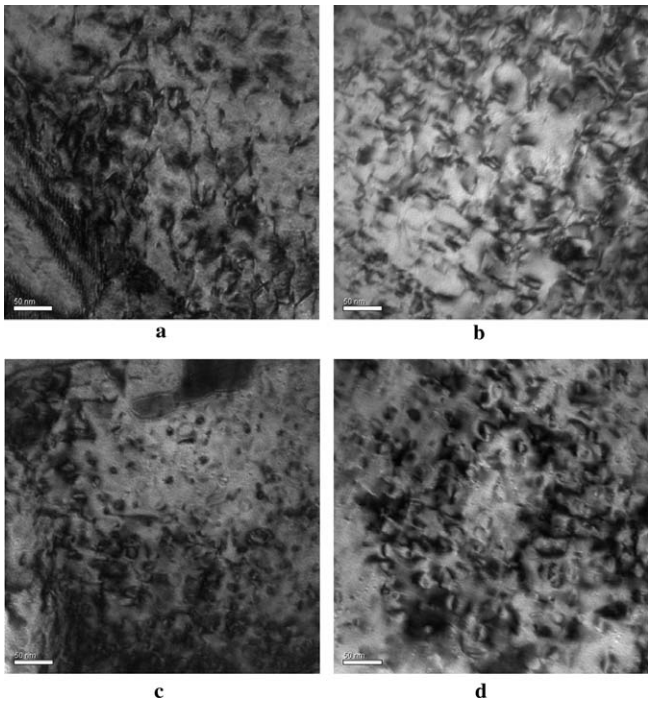

Fig. 4. Defect cluster structure of T91 samples irradiated at different conditions: (a) 3 dpa, 450 °C, (b) 10 dpa, 450 °C, (c) 3 dpa, 400 °C, and (d) 7 dpa, 400 °C.

Table 2
Irradiation conditions and defect data obtained from TEM investigation

Irradiation temperature (°C)	Dose (dpa)	Dislocation loop density ($\times 10^{21}$ m^{-3})	Dislocation loop size (nm)	Dislocation network density ($\times 10^{14}$ m^{-2})
400	3	9.10	28.5	8.14
400	7	13.93	31.8	13.90
400	10	14.00	49.0	21.50
450	3	1.30	10.5	0.45
450	10	1.73	12.8	0.72
500	3	3.60	60.0	6.78
500	7	4.10	64.5	8.30

be noted that the dislocation loop network features for the 450 °C irradiation (conducted on a different heat with a different heat treatment than the 400 °C and 500 °C irradiations), follow the same dose dependence, but have magnitudes that are considerably smaller.

3.2. Hardness

The results of hardness measurements on unirradiated and irradiated samples are presented in Table 3. In addition to the measured hardness level, Table 3 also contains the standard deviation and standard

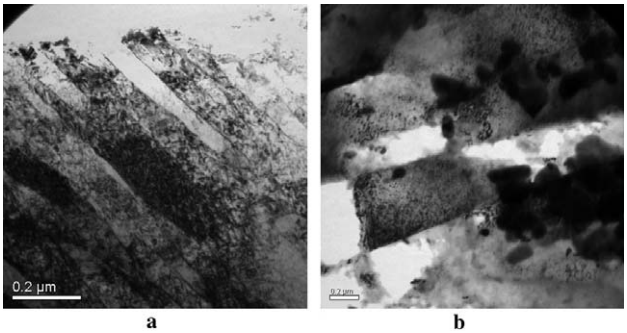

Fig. 5. TEM micrograph showing laths in T91 irradiated to 3 dpa at (a) 450 °C, and (b) 400 °C.

Table 3
Summary of results for hardness measurements on proton-irradiated T91

Dose (dpa)	Irradiation temp (°C)	Hardness (HV)	Std. dev.	Std. dev. of mean
0	–	210.2	4.24	0.85
3	400	238.2	8.35	1.67
5	400	366.2	7.91	1.58
7	400	370.2	8.57	1.70
10	400	374.3	9.94	1.98
3	450	314.2	25.6	5.00
7	450	330.6	29.3	5.90
10	450	382.6	38.5	7.70
3	500	230.3	7.23	1.45
7	500	241.4	6.53	1.30

deviation of the mean associated with the measurement. Note that while the standard deviation indicates the variability in the individual hardness measurements, the standard deviation of the mean indicates the variability in the mean sample hardness. The 7 dpa irradiation at 400 °C was divided in two irradiations of 2 and 5 dpa and hardness measurements were performed after 2 dpa irradiation. Also, no microstructural observations were made after 2 dpa.

The dose dependence of radiation-induced hardening for T91 is illustrated in Fig. 6(a). Hardening tends to saturate at a dose by 5 dpa at 400 °C. Results of irradiation-induced hardening as a function of temperature for different doses are shown in Fig. 6(b). Hardening is very sensitive to temperature and was minimal at 500 °C. Also, hardening is small at all temperatures at the lowest dose of 3 dpa. However, the 400 °C samples harden very rapidly above this dose and the amount and rate of hardening with dose decreases with increasing temperature.

3.3. Radiation-induced segregation (RIS)

Fig. 7(a) presents a representative grain boundary composition profile for a sample irradiated at 450 °C to 10 dpa. On average, Cr enriched by 4.7 wt%, V by 0.6 wt% (an enrichment by nearly 300%), and Fe depleted by 5.3 wt% over the bulk values. The full width at half maximum of the

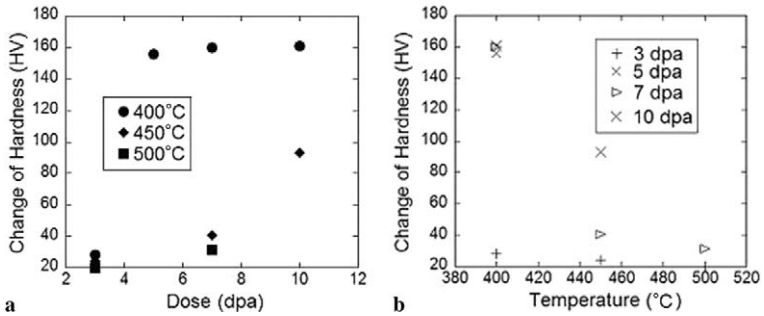

Fig. 6. (a) Dose dependence of hardening in T91 irradiated with 2 MeV protons, and (b) change in hardness following irradiation as a function of temperature.

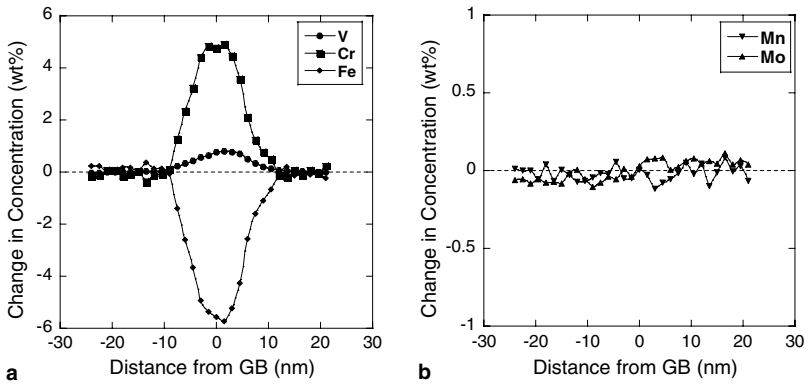

Fig. 7. Change in concentrations with distance from the GB for T91 irradiated to 10 dpa at 450 °C with 2.0 MeV protons. (a) Fe, Cr, and V, and (b) Mn and Mo.

Table 4
Average measured matrix and grain boundary concentrations for T91 irradiated to 10 dpa at 450 °C

	Fe	Cr	V	Mo	Mn
Matrix concentrations (wt%)					
Bulk composition	90.22	8.13	0.24	0.98	0.43
Calculated *k*-factors	1.45	1.00	0.24	0.94	0.47
Grain boundary concentrations (wt%)					
Average measured composition	84.97	12.71	0.91	1.00	0.41
Standard deviation	0.13	0.23	0.05	0.28	0.00
Standard deviation of mean	0.08	0.13	0.03	0.16	0.00

profiles is about 12 nm, which is very narrow and indicative of RIS. Results for Mn and Mo showed no significant variation in concentration across the grain boundary (GB), as shown in Fig. 7(b). The known bulk composition, calculated *k*-factors, and average measured GB compositions are presented in Table 4. No changes in composition were observed near the grain boundary in the unirradiated condition, which verifies that the segregation presented in Fig. 7(a) is fully due to radiation (RIS). Additionally, the RIS phenomenon appears to be confined to prior austenite grain boundaries as no segregation was observed at the lath boundaries of the 10 dpa sample.

4. Discussion

This section focuses on the development of microstructure and hardening as a function of irradiation dose and temperature and the relationship between the two. Radiation-induced segregation is also discussed.

4.1. Microstructure

The dislocation densities observed are comparable to those recently reported by Hashimoto and Klueh [4]. Hashimoto irradiated T91 with fast neutrons (HFIR) to 12 dpa at 400 °C. Analysis of dislocation microstructure revealed a dislocation loop population, with a density of approximately 5×10^{21} m^{-3}. T91 samples irradiated with 800 MeV protons in the SINQ-3 spallation neutron source at PSI also revealed dislocation loop populations [5]. Irradiation to a dose of 11.8 dpa at 360 °C resulted in a mean loop density of 1.3×10^{22} cm^{-3}. This is close to the dislocation density observed in T91 at 400 °C. The presence of large loops at 500 °C in T91 is similar to what was observed by Gan et al. [19] for Ni ion irradiated T91 at 500 °C. Loops with sizes up to 100 nm have been observed in the work by Gelles [2] on FFTF neutron irradiated T9 (similar to T91) at 420 °C to 200 dpa and also in 9Cr–2WV steels irradiated to 38 dpa at 420 °C by Klueh et al. [7]. Figs. 8(a) and (b) shows plots of our results and data from literature for dislocation loop size and loop density as a function of dose.

While the dependence of dislocation loop size, loop density and network density on dose for the 450 °C irradiation matches those for the 400 and 500 °C irradiations, the magnitudes are not consistent. This is likely due to the different heat treatment for Heat A irradiated to 450 °C as compared to that given to Heat B used for 400 and 500 °C irradiations. Heat A was tempered at a lower temperature,

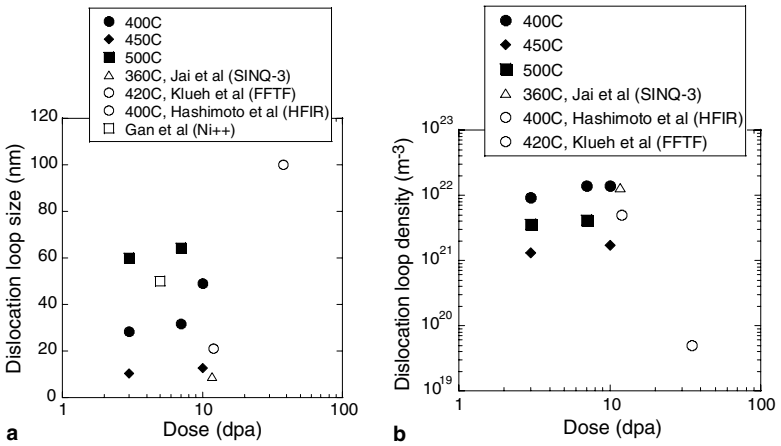

Fig. 8. Plot of (a) dislocation loop size as a function of dose and (b) dislocation loop density as a function of dose.

leading to reduced lath size, lower by a factor of 2.5 than that for Heat B. The reduced lath size means higher grain boundary area, which serves as a sink for irradiation-induced defects, suppressing initiation and slowing the growth of dislocation loops. Zinkle et al. [20] conducted similar studies on austenitic alloys and observed significant differences between dislocation evolution in cold worked and solution annealed steels at low doses (<10 dpa). They observed a lower loop density for the cold worked specimen. A reduced tempering temperature for Heat A would correspond to a state of higher degree of cold work from the standpoint of defect sinks. Note that Jai et al. [5] and Hashimoto and Klueh [4] irradiated T91 which was initially tempered at relatively lower temperatures of 760 and 700 °C, respectively and their data for dislocation loop size matches those for 450 °C irradiation in this study.

No cavities have been observed in the T91 irradiated with protons up to 10 dpa. Hashimoto and Klueh [4] report a population of 9 nm voids at a density of 3×10^{21} m^{-3} (0.17% swelling) in T91 irradiated in HFIR to 12 dpa at 400 °C (with 35 appm He). While this would appear to contradict the results from the proton irradiated alloys, swelling in ferritic–martensitic steels can also depend on heat treatment and tempering [21]. He gas would also help stabilize void nuclei thus it seems that the resultant swelling observed by Hasimoto and Klueh is due to the presence of He rather than due to defects produced from irradiation (He is not produced in proton irradiations). Further, 10 dpa is still a relatively low dose for swelling in ferritic/martensitic stainless steels. Data compiled by Klueh and Harries [21] show that void swelling in neutron irradiated commercial T91 steels ranges from 0.85% (~35 dpa at 420 °C) [20] up to only 2% after over 200 dpa at 420 °C [2].

No significant change was observed in the precipitate size and density following proton irradiation up to 10 dpa. This is consistent with the results from T91 alloys irradiated in HFIR [4] to 12 dpa at 400 °C where no difference in the size or distribution was measured for the $M_{23}C_6$ precipitates after irradiation. Was et al. [16] also confirmed that there was no change in precipitate size, distribution and structure after proton irradiation at 450 °C to 10 dpa.

4.2. Hardness

Klueh and Alexander performed tensile tests on 9Cr–1MoVNb (corresponding to T91) and 12Cr–1MoVW (corresponding to HT9) irradiated in HFIR (doses of 8–11 dpa and 37–72 dpa) and EBR-II (doses of ~16 dpa) [22]. The HFIR experiments showed that the yield strength increases occurred early in the radiation with only small changes occurring between 8–11 and 37–72 dpa. Yield strength changes were larger for the alloy with higher Cr concentration and for the thermal spectrum of HFIR. As changes in hardness and yield strength are proportional for metals [23], the hardness data of this work are consistent with the work of Klueh, with hardening increasing with bulk chromium concentration. Fig. 9 plots the change in yield strength vs. dose for various F–M alloys irradiated between 400 and 500 °C. Because hardening due to neutron irradiation is generally assessed by the change in yield strength, the hardening from microhardness measurements was compared to that from tensile tests using the relation $\Delta\sigma_y = 3.06\,\Delta H_v$ [23]. Note that hardening seems to saturate between 5 and 10 dpa for most of the alloys shown in Fig. 9.

Irradiation hardening resulting from proton irradiation at 400 °C and 500 °C was also measured in HCM12A, 11Cr ferritic–martensitic steel [24]. As with T91, the hardness increase at 400 °C saturates near 5 dpa and the hardness increase in HCM12A is similar in magnitude to the hardness increase for T91, Fig. 9. The increase in hardness is minimal at 500 °C for T91, consistent with the literature [21,25] and similar between HCM12A and T91 indicating that the temperature dependence of hardening is similar between the two alloys.

Irradiation hardening arises due to the formation of voids, precipitates, and/or dislocation loops that impede the motion of dislocation lines. The evolution of dislocation loops induced by irradiation can be rationalized by the formation of small glissile $1/2a_0\langle 1\,1\,1\rangle$ loops that, with increasing dose, will form sessile $a_0\langle 1\,0\,0\rangle$ loops that decorate the dislocation lines and eventually fill the matrix [26–28]. In the bcc lattice, the $a_0\langle 1\,0\,0\rangle$ loops are formed on the $(0\,0\,1)$ plane which is not a close-packed slip plane in the bcc lattice, resulting in immobile dislocation loops [29].

Microhardness values can be compared to calculations of the expected amount of hardening due to irradiated microstructure using the dispersed barrier hardening model. In this model, the hardening produced by a dispersion of obstacles in the glide plane is described by the relation between the increase in yield strength induced by the irradiation

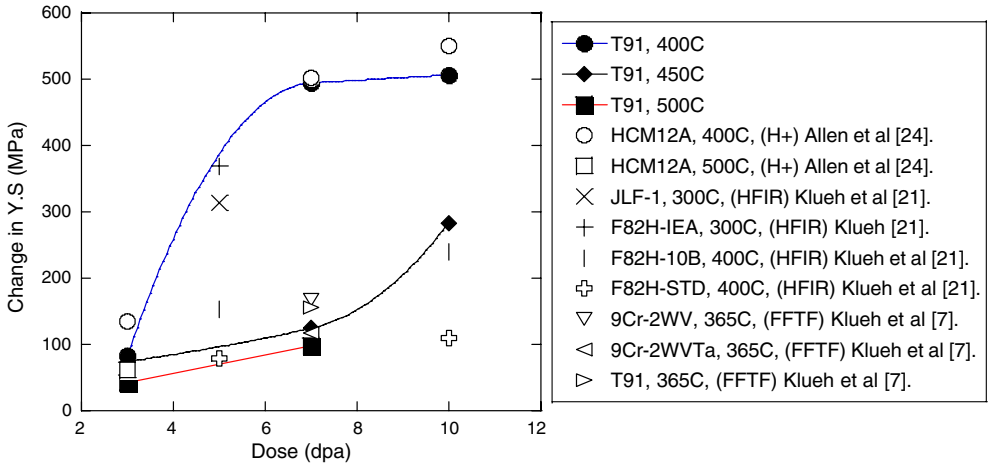

Fig. 9. Plot of change in yield strength vs. dose for various F–M alloys (solid symbols denote data in this study).

$\Delta\sigma = \sigma_{irr} - \sigma_{unirr}$ and a density of defect clusters N of diameter d according to [30]:

$$\Delta\sigma = M\mu\alpha b(Nd)^{1/2},$$

where μ is the shear modulus, b the burgers vector, M is the Taylor factor ($M = 3$ for bcc alloys [31]) and α is a parameter that describes the strength of the obstacle. For loops and other defect clusters, $\alpha \sim 0.2$–0.3.

Fig. 10(a) shows a plot of measured and calculated hardening for the irradiations described in Section 3.2. The calculated values are based on the dislocation loop density. Note that while the trends are the same, the magnitudes of the measured hardening at 400 °C and 450 °C far exceed that calculated from the microstructure at higher dose. At 500 °C the magnitude of the calculated hardening matches that of measured hardening even at higher dose. Fig. 10(b) accounts for the various microstructure contributions to hardness for the case of 450 °C. Note that on top of the hardness of the unirradiated matrix, the visible dislocation loops structure and the dislocation network add nearly equal increments of hardening that increase rapidly with dose to 3 dpa. Hardening due to black dots [32] seems to increase with dose up to a low dose of around 0.1 dpa and then saturates with dose. Note that the nano-sized black dot density was not measured quantitatively and the hardening represented due to them is on qualitative basis. At 3 dpa, the hardening accounted for by the observed dislocation loops and network structure exceeds the measured hardening. However, above 3 dpa, the measured hardening increases linearly with dose while the hardening accounted for by the observable dislocation structure has nearly saturated. By 10 dpa, the observable

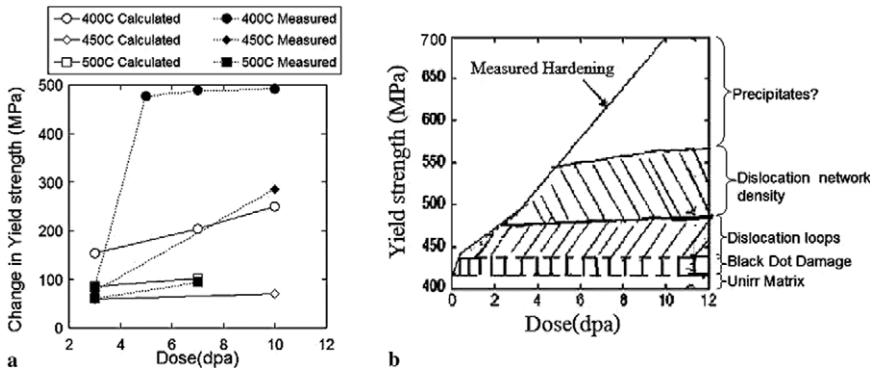

Fig. 10. (a) Plot of irradiation hardenings determined by microhardness indentation (closed symbols) and calculated from the dispersed barrier hardening model (open symbols). (b) Schematic showing various microstructure contributions to hardness for the alloy irradiated at 450 °C.

dislocation structure accounts for only half of the measured hardening, indicating that additional microstructure changes have occurred that are not visible in the TEM. Likely candidates are nano-sized precipitates, possibly Cu being a constituent, even though it is present in small percentage by weight and small dislocation loops (<1 nm) that can significantly harden the matrix.

4.3. Radiation-induced segregation

Radiation-induced segregation (RIS) is a non-equilibrium process that is due to the unequal participation of solutes in the vacancy and interstitial defect fluxes. Segregation occurs when a given alloying component has a preferential association with the defect flux. Enrichment or depletion of each element occurs according to the relative interaction of each element with the defect flux. The inverse Kirkendall effect [33,34] has been used to successfully describe RIS in austenitic stainless steels under irradiation, in which Ni enriches and Cr depletes at GBs and Fe either enriches or depletes depending on the bulk alloy composition.

Very few studies of RIS in ferritic–martensitic alloys have been published. Ohnuki et al. observed Cr enrichment in Fe–13Cr and Fe–13Cr–1Si irradiated to 57 dpa with 200 keV C+ ions [36]. However, they observed Cr depletion in Fe–13Cr–1Ti in the same study and in electron irradiated Fe–13Cr (without the presence of additional C) [37]. Allen et al. [35] have observed significant Cr enrichment in HCM12A irradiated with protons at 400 °C and at 500 °C to doses between 3 and 10 dpa, which increased with dose. Segregation is greatest at grain boundaries but is also observed on cleavage facets created by fracture in an Auger electron spectrometer (AES) chamber. Additionally, Allen observed GB enrichment of chromium in the unirradiated condition. However, AES measurements also include pre-existing grain boundary carbides which are a likely the source of this apparent enrichment. Our results show that in the unirradiated condition, T91 exhibits no GB enrichment or depletion of Cr or Fe. Therefore, any changes measured after irradiations are due to RIS.

Since Cr and V generally act as oversized solutes in the Fe one expects the inverse Kirkendall effect would predict that Cr and V should deplete at the grain boundary by preferential exchange with vacancies. The results of the present work, that of Allen et al., and that of Ohnuki et al. suggest that either a mechanism other than inverse Kirkendall is controlling segregation in this alloy or the difference in migration energies in BCC dictates that Fe diffuses away from the GB at a faster rate than Cr. Ohnuki et al. suggested that a Cr-interstitial solute (such as C)-vacancy complex could lead to the enrichment of Cr at the GB in Fe–13Cr and Fe–13Cr–1Si. Ohnuki's C+ irradiation resulted in the implantation of about 0.024 wt% C at a dose (57 dpa) at which they observed Cr enrichment. The C content of T91 Heat A was 0.09 wt% which is significant compared to the implanted C level in Ohnuki's experiment. Ohnuki explains the depletion of Cr in Fe–13Cr–Ti as being due to the addition of Ti that acted to suppress segregation.

However, Brimhall et al. observed no measurable segregation of any major or minor alloying element, apart from phosphorus, in HT-9 (Fe–12Cr–1Mo–0.2C) irradiated with 5 MeV Ni^{++} [38] to doses <1 dpa. Also, the Cr enrichment profiles observed by Ohnuki are 100–200 nm wide, which is one order of magnitude greater than those generally observed for RIS. The electron irradiation experiment is also suspect as there is significant evidence of unusual behavior in electron irradiation experiments due to the intense damage zone created by the electron beam.

Allen et al. [35] have applied the modified inverse Kirkendall (MIK) model to Fe–10.5Cr–0.4Ni (HCM12a) and predicted Cr enrichment, which is consistent with both the present work and their RIS measurements. Although this model was tested against a large database of measurements in austenitic alloys, the model calculates migration energies based on pair potentials so no artifacts from the FCC structure are used in the calculation for BCC materials. Clearly, further study is necessary to fully understand RIS in ferritic–martensitic alloys.

5. Conclusions

(1) The observed dislocation loop size and loop density increased with increasing dose at constant temperature. For a given dose, the observed dislocation loop size increased with increasing temperature, while the loop density decreased. No change in precipitate or lath size occurred with irradiation and no voids were observed. Overall, the proton irradiated microstructure is consistent with reactor and spallation system experiments.
(2) The evolution of the irradiated microstructure is highly dependent upon the alloy heat treat-

ment. Lower tempering temperature results in smaller laths and a greater sink density, suppressing both nucleation and growth of dislocation loops.

(3) The change in hardness increases with increasing dose and decreases with increasing irradiation temperature. For low-temperature (400 °C), the change in hardness saturates by 5 dpa.

(4) The difference between measured and calculated hardening is likely due to irradiation-induced precipitation and perhaps black dots that are below the resolution limits of TEM imaging.

(5) Grain boundary microchemistry measurements have shown radiation-induced enrichment of Cr and V and depletion of Fe at grain boundaries in T91, opposite of the trend observed for FCC austenitic stainless steels. Additionally, RIS is confined to prior-austenite grain boundaries as it is not observed at martensite lath boundaries.

Acknowledgements

Support for this work was provided by the United States Department of Energy under the NERI (U. Wisconsin. No. A824316), INERI (Contract No. 3F-01041), AFCI (LANL contract 73713-001-03 8T) and the AFCI Fellowship program. The authors gratefully acknowledge the facilities provided by the Electron Microbeam Analysis Laboratory and Michigan Ion Beam Laboratory at the University of Michigan, and the Oak Ridge National Laboratory Shared Research Equipment (ShaRE) program (sponsored by the Division of Materials Sciences and Engineering, US Department of Energy, under contract DE-AC05-00OR22725 with UT-Battelle, LLC). The authors would also like to thank Ovidiu Toader and Victor Rotberg of the Michigan Ion Beam Laboratory for their invaluable support in conducting the irradiations and Ed Kenik, Jim Bentley and Neal Evans of ORNL for access to and assistance with STEM/EDS on the Philips CM200 TEM.

References

[1] R.L. Klueh, in: Proceedings of the Symposium on Materials for Spallation Neutron Sources, The Minerals, Metals, & Materials Society, 1997, p. 67.
[2] D.S. Gelles, J. Nucl. Mater. 233–237 (1996) 293.
[3] J.J. Kai, R.L. Klueh, J. Nucl. Mater. 230 (1996) 116.
[4] N. Hashimoto, R.L Klueh, J. Nucl. Mater. 305 (2002) 153.
[5] X. Jia et al., J. Nucl. Mater. 318 (2003) 207.
[6] B.H. Sencer et al., J. Nucl. Mater. 307–311 (2002) 266.
[7] R.L. Klueh et al., J. Nucl. Mater. 225 (1995) 175.
[8] S.A. Maloy et al., J. Nucl. Mater. 296 (2001) 119.
[9] M.B. Toloczko et al., J. Nucl. Mater. 318 (2003) 200.
[10] Y. Dai et al., J. Nucl. Mater. 318 (2003) 192.
[11] K. Farrell, T.S. Byun, J. Nucl. Mater. 296 (2001) 129.
[12] K. Farrell, T.S. Byun, J. Nucl. Mater. 318 (2003) 274.
[13] P. Jung et al., J. Nucl. Mater. 318 (2003) 241.
[14] G.S. Was, J.T. Busby, T.R. Allen, E.A. Kenik, A. Jenssen, S.M. Bruemmer, J. Gan, A.D. Edwards, P. Scott, P.L. Andresen, J. Nucl. Mater. 300 (2002) 198.
[15] J.F. Ziegler, SRIM 2003 Program, J.P. Biersack, IBM Corporation, Yorktown, NY, 2003.
[16] G.S. Was, J.T. Busby, T.R. Allen, J. Gan, Proceedings of the Accelerator Applications Division Topical Meeting of the 2003 ANS Annual Meeting, 2003, p. 864.
[17] T.R. Allen, D.L. Damcott, G.S. Was, E.A. Kenik, in: Proceedings of the Seventh Environmental Degradation, NACE International, Houston, TX, 1995, p. 997.
[18] D.B. Williams, C.B. Carter, Transmission Electron Microscopy, Plenum, New York, NY, 1996.
[19] J. Gan, T.R. Allen, J.I. Cole, S. Ukai, S. Shuttanandan, S. Thevuthasan, Mater. Res. Soc. Symp. Proc. 792 (2004).
[20] S.J. Zinkle et al., J. Nucl. Mater. 206 (1993) 266.
[21] R.L. Klueh, D.R. Harries, High-chromium Ferritic and Martensitic Steels for Nuclear Applications, MONO3, American Society for Testing and Materials, Philadelphia, 2001.
[22] R.L. Klueh, D.J. Alexander, J. Nucl. Mater. 187 (1992) 60.
[23] J.T. Busby, M.C. Hash, G.S. Was, J. Nucl. Mater. 336 (2005) 267.
[24] T.R. Allen, L. Tan, J.D. Tucker, J. Gan, G. Gupta, G.S. Was, J. ASTM Int. 2 (3) (2005).
[25] W.L. Hu, D.S. Gelles, in: F.A. Garner, C.H. Henager Jr., N. Igata (Eds.), Influence of radiation on material properties: 13th International Symposium, ASTM STP 956, Part 2, 1987, p. 83.
[26] J. Marian, B.D. Wirth, R. Schaublin, G.R. Odette, J.M. Perlado, J. Nucl. Mater. 323 (2003) 181.
[27] J. Marian, B.D. Wirth, Phys. Rev. Lett. 88 (25) (2002) 1.
[28] N. Baluc, R. Schaublin, P. Spatig, M. Victoria, Effects of radiation on materials: 21st International Symposium, ASTM STP 1447, 2004.
[29] G.E. Dieter, Mechanical Metallurgy, Mcgraw-Hill, 1986, p. 165.
[30] A.L. Bement, in: Proceedings of the Second International Conference on Strength of Metals and Alloys, ASM International, 1973, p. 693.
[31] U.F. Kocks, Metall. Trans. 1 (1970) 1121.
[32] R. Schaeublin, D. Gelles, M. Victoria, J. Nucl. Mater. 307–311 (2002) 197.
[33] T.R. Allen, G.S. Was, Acta Mater. 46 (10) (1998) 3679.
[34] T.R. Allen et al., J. Nucl. Mater. 255 (1998) 44.
[35] Allen et al., this Proceedings, 2005.
[36] S. Ohnuki et al., J. Nucl. Mater. 103&104 (1981) 1121.
[37] H. Takahashi et al., J. Nucl. Mater. 103&104 (1981) 1415.
[38] J.L. Brimhall et al., J. Nucl. Mater. 122&123 (1984) 196.